Joule

CellPress

Article

The nature of dynamic local order in $CH_3NH_3PbI_3$ and $CH_3NH_3PbBr_3$

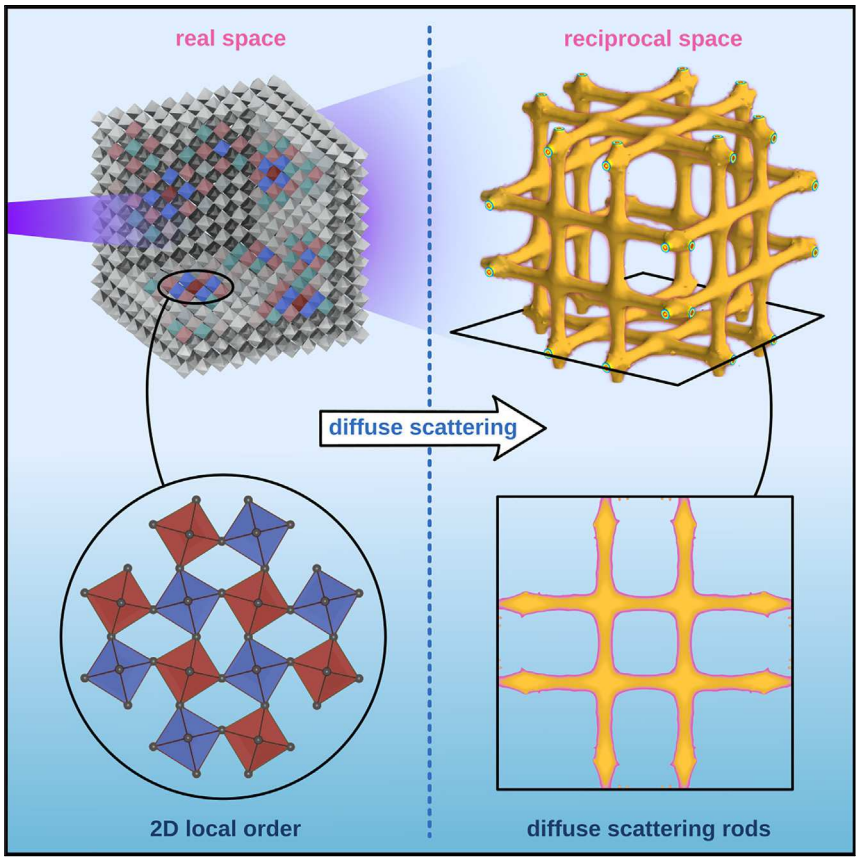

The cubic structure of $CH_3NH_3PbI_3$ and $CH_3NH_3PbBr_3$ is composed of short-range structural correlations, primarily two-dimensional, as revealed by experimental and computational diffuse scattering analysis. This work completes the first step toward understanding the structure-property-function relationship of hybrid lead-halide perovskites. Furthermore, we make connections between the observed structure and the remarkable optoelectronic properties of, and detrimental ion migration within, these materials.

Nicholas J. Weadock, Tyler C. Sterling, Julian A. Vigil, ..., Hemamala I. Karunadasa, Dmitry Reznik, Michael F. Toney

nicholas.weadock@colorado.edu (N.J.W.)
dmitry.reznik@colorado.edu (D.R.)
michael.toney@colorado.edu (M.F.T.)

Highlights

Cubic $CH_3NH_3PbI_3$ and $CH_3NH_3PbBr_3$ are composed of lower-symmetry structural correlations

Two-dimensional regions of dynamic tilting in PbX_6 octahedra are several unit cells wide

Correlations of a similar size are also observed in the organic-cation sublattice

These correlations have a direct impact on optoelectronic properties and ion migration

Weadock et al., Joule 7, 1–16
May 17, 2023
https://doi.org/10.1016/j.joule.2023.03.017

Please cite this article in press as: Weadock et al., The nature of dynamic local order in $CH_3NH_3PbI_3$ and $CH_3NH_3PbBr_3$, Joule (2023), https://doi.org/10.1016/j.joule.2023.03.017

Joule

CellPress

Article

The nature of dynamic local order in $CH_3NH_3PbI_3$ and $CH_3NH_3PbBr_3$

Nicholas J. Weadock,[1,2,16,17,*] Tyler C. Sterling,[3,16] Julian A. Vigil,[4,5] Aryeh Gold-Parker,[5] Ian C. Smith,[5] Ballal Ahammed,[6] Matthew J. Krogstad,[7] Feng Ye,[8] David Voneshen,[9,10] Peter M. Gehring,[11] Andrew M. Rappe,[12] Hans-Georg Steinrück,[13] Elif Ertekin,[6] Hemamala I. Karunadasa,[5,14] Dmitry Reznik,[3,*] and Michael F. Toney[1,2,15,*]

SUMMARY

Hybrid lead-halide perovskites (LHPs) are semiconductors with novel properties that are distinctively governed by structural fluctuations. Diffraction experiments sensitive to long-range order reveal a cubic structure in the device-relevant, high-temperature phase. Local probes find additional short-range order with lower symmetry that may govern structure-function relationships. However, our understanding is impeded by unresolved dimensionality, participating atoms, and dynamics of short-range order. Here, we determine the true structure of two hybrid LHPs, $CH_3NH_3PbI_3$ and $CH_3NH_3PbBr_3$, using a combination of single-crystal diffuse scattering, neutron inelastic spectroscopy, and molecular dynamics simulations. The remarkable collective dynamics, not observed in previous studies, consist of a network of local, two-dimensional, circular regions of dynamically tilting lead-halide octahedra (lower symmetry) that induce longer-range intermolecular $CH_3NH_3^+$ correlations. The dynamic local structure may introduce transient ferroelectric or antiferroelectric domains that increase charge carrier lifetimes and strongly affect halide migration, a poorly understood degradation mechanism.

INTRODUCTION

The crystal structure and associated symmetry of a material are key determinants of mechanical, electronic, optical, and thermal properties. One has to look no further than seminal condensed matter physics textbooks for derivations of these properties made possible by consideration of the long-range or average order determined by the crystal lattice and translational symmetry.[1,2] However, in many materials, including disordered rocksalts and intercalation compounds used for battery cathodes, relaxor ferroelectrics, thermoelectrics, and oxide and halide perovskites, the important properties are not well described by the long-range structure. Instead, it is short-range order that dominates aspects of the structure-function relationship.[3–10] In scattering experiments, short-range or local order manifests as diffuse scattering, a result of static and dynamic deviations from the average structure. Fixed chemical or local structural correlations result in static diffuse scattering, whereas thermal diffuse scattering arises from dynamic displacements due to lattice dynamics.[11] In an analogous fashion, short-range magnetic correlations generate magnetic diffuse scattering observable with neutron scattering.[12] Resolving structural correlations in disordered materials has recently become more feasible with the development of high-flux, single-crystal X-ray diffuse scattering (XDS) and

CONTEXT & SCALE

Hybrid organic-inorganic lead-halide perovskites (LHPs) are a class of semiconductors with remarkable properties relevant to optoelectronic applications. The structure-property-function relationship in LHPs, however, is poorly understood, leading to incomplete descriptions of optoelectronic properties and a persistent problem of device degradation due to ion migration. Here, we reveal the true structure to contain an assembly of dynamic, two-dimensional short-range structural correlations in the lead-halide octahedral sublattice, with additional correlations between organic molecules.

We propose that these correlations are the origin of large-amplitude halide displacements, which govern charge carrier mobility and the sharpness of the absorption edge. Correlations between organic molecules may introduce regions of transient ferroelectricity or antiferroelectricity, which increase charge carrier lifetime. Finally, the correlations introduce an ion diffusion barrier that is static on the timescale of diffusive jumps.

neutron diffuse scattering (NDS) instruments and sophisticated modeling algorithms,[5,13–17] opening up enormous opportunities to understand how local order impacts materials properties. Combining XDS and NDS reveals additional information about short-range order in materials with both light and heavy elements.[18]

Organic-inorganic metal halide perovskites are a recently re-invigorated class of semiconductors with remarkable optoelectronic performance that defies traditional intuition. Hybrid lead halide perovskites (LHPs) possess a mechanically soft, defect-tolerant crystal lattice with strong structural disorder and mobile ions at modest temperatures.[19] Fluctuations in orbital overlap arising from large thermal displacements of iodide in methylammonium ($CH_3NH_3^+$, $CD_3ND_3^+$ = MA^+) lead iodide directly influence the temperature dependence of the electron (or hole) mobility and optical band gap.[20] X-ray and neutron diffraction measurements, which probe long-range order, report that the high-temperature phase is cubic, with well-defined Bragg peaks.[21–23] This cubic perovskite structure is shown in Figure 1A and consists of corner-sharing PbX_6 (X = I^-, Br^-) octahedra surrounding a dynamically disordered MA^+ cation within the cuboctahedral interstice. Measurements probing short-range order in the high-temperature phase, however, suggest the local structure is of lower symmetry.[24–28] The lack of consensus regarding the exact symmetry and dynamics of this enigmatic local structure limits our understanding and control of optoelectronic properties and ion migration in LHPs. Short-range order arising from dynamic, two-dimensional (2D) correlations of lead bromide octahedra has recently been identified in $CsPbBr_3$.[6] These correlations are most prominent in the cubic phase above 433 K and may not play a significant role in $CsPbBr_3$-based device operation. The significance and prevalence of such correlations in hybrid LHPs, including contributions from the organic cations, is not resolved.

Organic cation and halide anion migration in LHPs, especially under illumination, is detrimental to device performance and stability, yet the origin is not well understood. Consequences of ion migration include formation of space charge potentials at interfaces, accelerated degradation and loss of constituent elements, and light-induced phase segregation in mixed-halide compositions.[30] A complete picture of the high-temperature structure and dynamics is essential to model ion migration pathways accurately.[31] It is also important to characterize the short-range order in the organic sublattice, as the rotating MA^+ molecular dipoles may screen band-edge charge carriers and extend carrier lifetimes.[32]

We use single-crystal XDS, NDS, and neutron spectroscopy, combined with molecular dynamics (MD) simulations, to uncover the true structure and dynamics of the nominally simple cubic ($Pm\bar{3}m$) phases of $MAPbI_3$ (>328 K) and $MAPbBr_3$ (>236 K). We find that the cubic phase (Figures 1A and 1C) is composed of dynamic, roughly circular 2D "pancakes" of tilted lead-halide octahedra, which align along any of the three principal axes of the cubic structure and (Figures 1B and 1D) induce additional structural correlations of the organic sublattice within the layers sandwiching the octahedra. Taken together, these regions of dynamic local order are several unit cells in diameter with lifetimes on the order of several picoseconds, resulting in a dynamic landscape for charge carriers and ion migration. This extended dynamic local order was neither observed nor predicted in previous studies of structural dynamics in hybrid LHPs.[33–36] Embedded within this dynamic structure we find additional static three-dimensional (3D) droplets of the intermediate tetragonal phase, consistent with previous reports.[25,27] The structural correlations in the MA^+ sublattice are a unique characteristic in these hybrid systems, with the implications discussed below.

[1]Materials Science and Engineering, University of Colorado, Boulder, Boulder, CO 80303, USA

[2]Department of Chemical and Biological Engineering, University of Colorado, Boulder, Boulder, CO 80303, USA

[3]Department of Physics, University of Colorado, Boulder, Boulder, CO 80303, USA

[4]Department of Chemical Engineering, Stanford University, Stanford, CA 94305, USA

[5]Department of Chemistry, Stanford University, Stanford, CA 94305, USA

[6]Department of Mechanical Science & Engineering and Materials Research Laboratory, University of Illinois at Urbana-Champaign, Urbana, IL 61801, USA

[7]Advanced Photon Source, Argonne National Laboratory, Lemont 60439, IL, USA

[8]Neutron Scattering Division, Oak Ridge National Laboratory, Oak Ridge, TN 37830, USA

[9]ISIS Facility, Rutherford Appleton Laboratory, Didcot OX11 0QX, UK

[10]Department of Physics, Royal Holloway University of London, Egham TW20 0EX, UK

[11]NIST Center for Neutron Research, National Institute of Standards and Technology, Gaithersburg, MD 20899, USA

[12]Department of Chemistry, University of Pennsylvania, Philadelphia, PA 19104, USA

[13]Department Chemie, Universtät Paderborn, Paderborn, Germany

[14]Stanford Institute for Materials and Energy Sciences, SLAC National Accelerator Laboratory, Menlo Park, CA 94025, USA

[15]Renewable and Sustainable Energy Institute (RASEI), University of Colorado, Boulder, Boulder, CO 80303, USA

[16]These authors contributed equally

[17]Lead contact

*Correspondence: nicholas.weadock@colorado.edu (N.J.W.), dmitry.reznik@colorado.edu (D.R.), michael.toney@colorado.edu (M.F.T.)

https://doi.org/10.1016/j.joule.2023.03.017

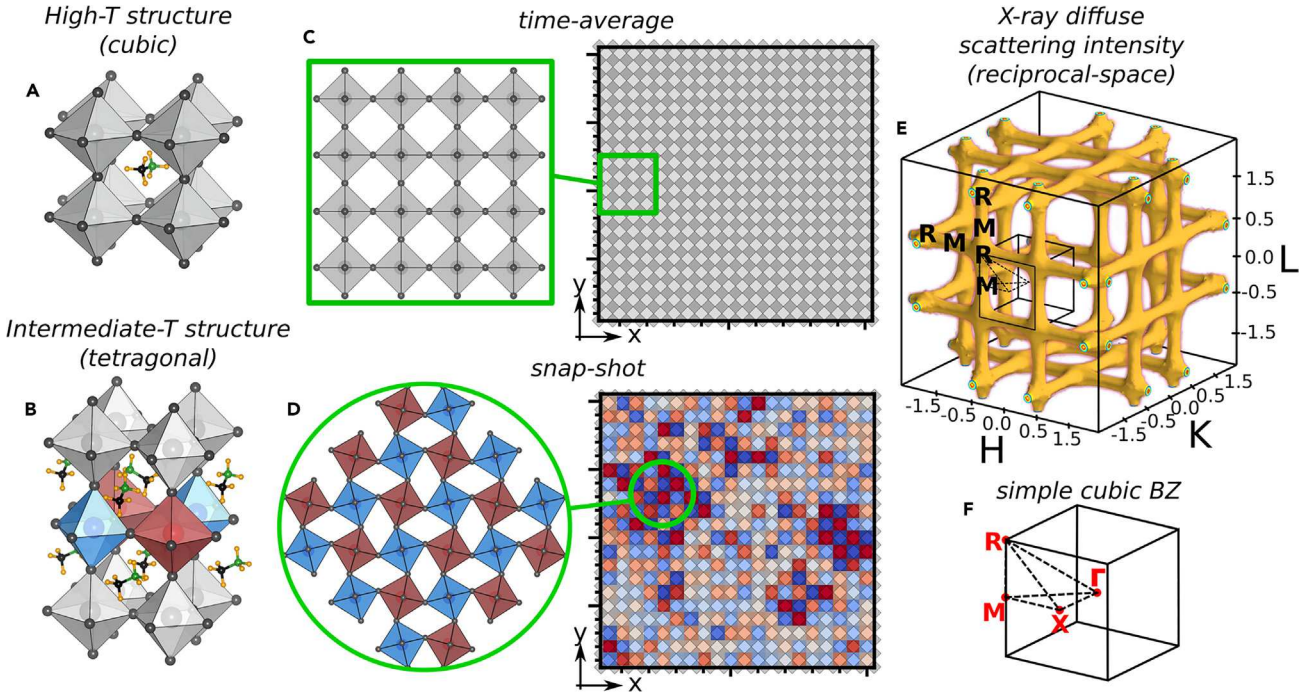

Figure 1. Summary of real-space and reciprocal space manifestations of local correlations in LHPs

(A–C) Visualizations of the high-temperature cubic structure (A and C) and the intermediate-temperature tetragonal structure (B) of $MAPbI_3$ and $MAPbBr_3$. MA^+ disorder has been omitted for clarity. The cubic-tetragonal transition in $MAPbI_3$ and $MAPbBr_3$ occurs at 328 and 236 K, respectively, by the freezing out of octahedral tilts in an out-of-phase pattern.[22,29]

(D) Instantaneous snapshots of the cubic structure from MD reveal dynamic, two-dimensional correlations consisting of tilted PbX_6 octahedra that can orient perpendicular to any of the three principal axes.

(E) Three-dimensional visualization of the X-ray diffuse scattering intensity generated by the structural correlations. The diffuse volume is indexed by Miller indices H, K, L, of which integer values enumerate each Brillouin zone (BZ).

(F) The simple cubic BZ with high symmetry points indicated in red. The diffuse rods in (E) run along the BZ edge, connecting M and R points.

RESULTS AND DISCUSSION

The experimental scattering function $S(\mathbf{Q})$ in the cubic phase of $MAPbI_3$ at 345 K is shown in Figure 2. Specifically, we present the L = 0.5, 1.5 planes measured with both XDS (Figures 2A and 2C, left) and NDS (Figures 2B and 2D, left). $S(\mathbf{Q})$ calculated from atomic trajectories obtained with MD simulations of $MAPbI_3$ (see experimental procedures) is plotted in the right-hand panels of Figures 2A–2D and both panels of Figures 2G and 2H for comparison. The experimental $S(\mathbf{Q})$ in the cubic phase of $MAPbBr_3$ at 250 K is plotted in Figure S1 and shows diffuse scattering intensity for XDS and NDS that are nearly identical to $MAPbI_3$.

Our approach to solving the true structure of the nominally simple cubic $MAPbI_3$ and $MAPbBr_3$ involves decomposing the observed diffuse scattering profile into four components and analyzing their energy and $\mathbf{Q}$-dependence. These components include: (1) rods of constant (XDS) or varied (NDS) intensity spanning the Brillouin zone (BZ) edge (M-R direction in Figure 1, $q = [0.5, 0.5, l]$); (2) an additional contribution centered at the R-point [$q = (0.5, 0.5, 0.5)$]; (3) broad intensity centered at the X-point [$q = (0.5, 0, 0)$] observed previously and discussed in the supplemental information; and (4) contributions from the MA^+ sublattice deduced from the alternating diffuse rod intensity profile observed in NDS but not XDS. This difference between XDS and NDS is highlighted by the one-dimensional linecuts through the XDS and NDS data shown in Figures 2E and 2F. Specifically, the peaks at K = $\pm$ 2.5

Please cite this article in press as: Weadock et al., The nature of dynamic local order in $CH_3NH_3PbI_3$ and $CH_3NH_3PbBr_3$, Joule (2023), https://doi.org/10.1016/j.joule.2023.03.017

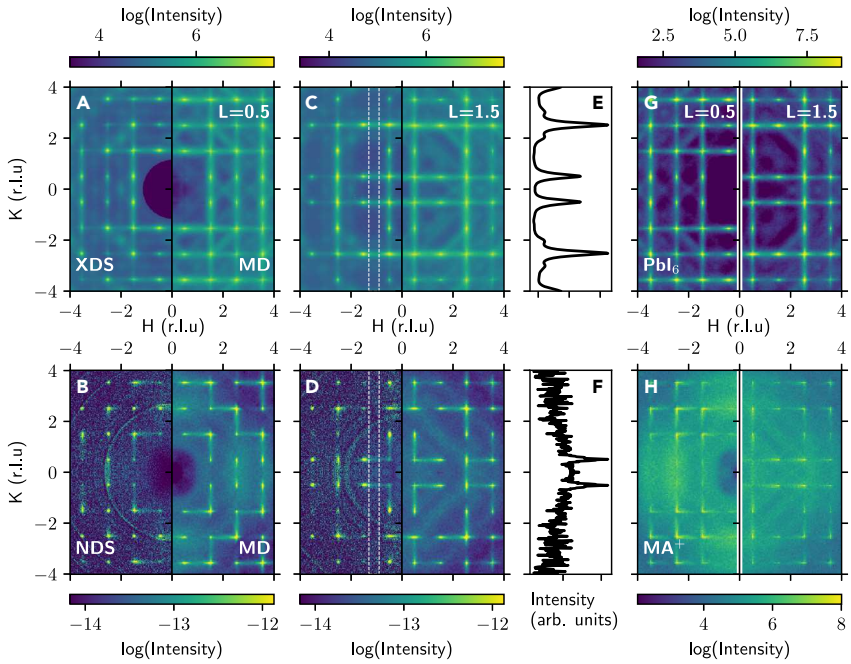

Figure 2. Diffuse scattering rods in $MAPbI_3$

Experimental $S(\mathbf{Q})$ for $MAPbI_3$ measured with XDS (A and C, left panels) and NDS (B and D, left panels) at 345 K. The XDS data are inherently energy integrated whereas the NDS data are static, with a 0.9 meV full width at half-maximum (FWHM) energy bandwidth.

(A–H) (A and B) correspond to the L = 0.5 plane, and (C and D) the L = 1.5 plane. No Bragg intensity is expected in these half-order planes; therefore, any intensity is diffuse scattering. The faint circular rings in the experimental NDS data are residual Debye-Scherrer diffraction rings from the aluminum sample holder. Theoretical $S(\mathbf{Q})$, calculated from MD simulations ($\pm$1 meV bandwidth), are plotted in the right panels of (A)–(D). In (A) and (C), X-ray form factors were used whereas (B, D, G, and H) were calculated using neutron scattering lengths (see supplemental information). In (E) and (F), plots of one-dimensional linecuts along K, integrating 0.7:H:1.3 and 1.4:L:1.6, highlight the differences between XDS and NDS. In (G) and (H), individual contributions from PbI_6 and MA^+ to the calculated neutron $S(\mathbf{Q})$, respectively, are plotted with the left panels corresponding to L = 0.5 and the right panels to L = 1.5. We note that the NDS plotted here corresponds to the elastic scattering channel of the CORELLI spectrometer ($\sim$ 0.9 meV FWHM for E_i = 30 meV[17]).

originating from the corresponding diffuse rod along the H direction in XDS (Figure 2E) are not observed in NDS (Figure 2F). Our analysis is complemented by MD simulations of $MAPbI_3$, which reproduce the experimental diffuse scattering. The experimental and calculated XDS (Figure 2) show remarkable agreement: comparing the two results in a root-mean-square error of 3.6% (see Figures S2 and S3 and related discussion) after adjusting only the background and scaling of the calculated $S(\mathbf{Q})$. The agreement between the experimental and calculated NDS is very good; however, there are small differences in intensities highlighted in Figure S4 that likely arise from the classical potentials used here. Given the good agreement, we examine the real-space structure simulated with MD to determine the origin of the diffuse scattering.

The XDS rods of diffuse scattering have constant intensity along the entire BZ edge (Figure S5) and a width larger than the instrument resolution ($\approx$0.02 Å^{-1}). This lineshape arises from 2D structural correlations in real-space. We show these correlations in Figure 3, which presents a simplified visualization of the MD simulation. These plots track PbI_6 octahedral rotations, defined by an azimuthal rotation angle φ about the [001] (Figures 3A and 3B) or [010] (Figures 3C and 3D) directions.

Please cite this article in press as: Weadock et al., The nature of dynamic local order in $CH_3NH_3PbI_3$ and $CH_3NH_3PbBr_3$, Joule (2023), https://doi.org/10.1016/j.joule.2023.03.017

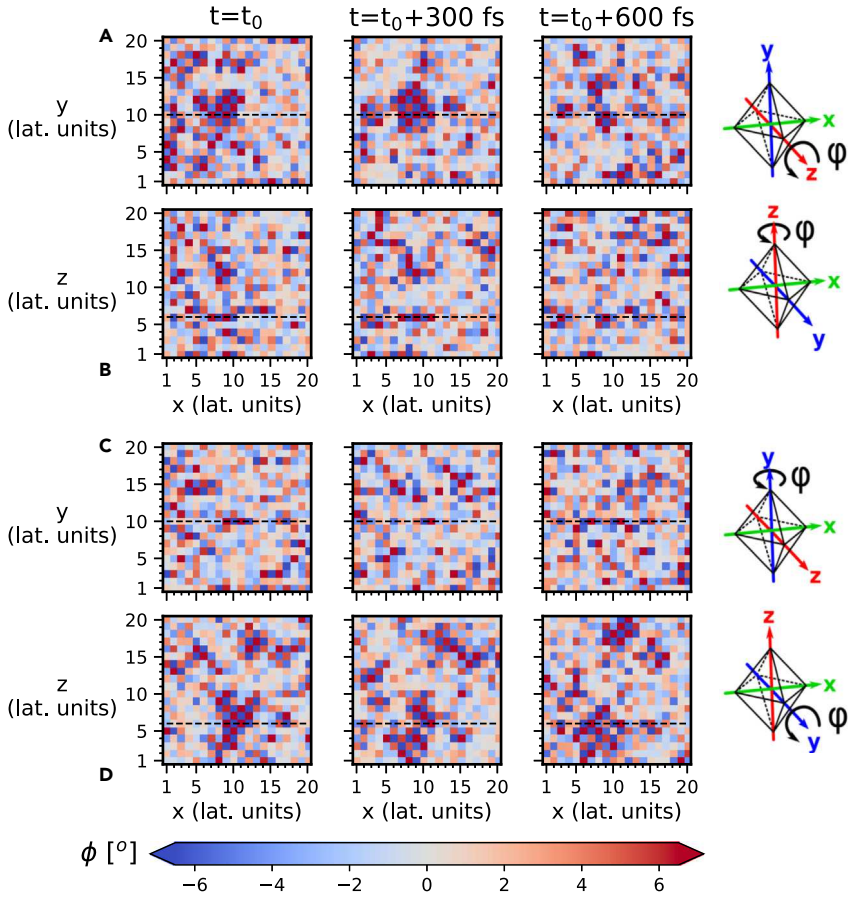

Figure 3. Spatiotemporal dynamics of PbI_6 octahedral rotations in cubic $MAPbI_3$

Each pixel encodes the octahedral rotation angle φ about the z axis (A and B) and the y axis (C and D). The columns are offset in time by Δ t = 300 fs to highlight the dynamic nature. The top rows (A) and (C) are in the *x-y* plane and the bottom rows (B) and (D) are in the *x-z* plane. In (A) and (D), the rotation is about the axis perpendicular to the plane, as shown by the diagrams on the right. In (B) and (C), the rotation is about an axis parallel to the figures' vertical axis. The dashed lines indicate the intersection between the *x-y* plane in (A) and (C) and the *x-z* plane in (B) and (D). Note that the two-dimensional regions visible in (A) and (D) are one unit-cell thick in the normal direction (B and C).

Correlated regions of alternating large tilts are identified by neighboring red and blue pixels (representing octahedra) in Figures 3A and 3D. Along the axis of rotation indicated in the corresponding schematic, the tilts are uncorrelated between planes (Figures 3B and 3C), revealing the existence of 2D pancakes of tilted octahedra with a diameter on the order of 5 unit cells. These regions are reminiscent of the tilts associated with the tetragonal structure in Figure 1B. The tilts generate in-plane antiphase structural correlations with a periodicity of 2*a*. The associated wave vector of the correlation is $q = 2\pi/2a = \pi/a$, which is the zone boundary for the simple cubic BZ. The tilted regions are confined to a single PbI_6 sheet and therefore the diffuse scattering intensity manifests as rods. The same structural correlations are present in the cubic phase of $MAPbBr_3$ because the XDS and NDS are qualitatively identical to that of $MAPbI_3$ (Figures S1 and S4).

Intermolecular structural correlations in the MA^+ sublattice are implied from the alternating intensity pattern of the diffuse rods present in NDS but not XDS. The

Please cite this article in press as: Weadock et al., The nature of dynamic local order in $CH_3NH_3PbI_3$ and $CH_3NH_3PbBr_3$, Joule (2023), https://doi.org/10.1016/j.joule.2023.03.017

MA^+ correlations are explored in the calculated $S(\mathbf{Q})$ in Figures 2G, 2H, and S6–S8. Specifically, we set the neutron scattering lengths of Pb and I to zero in the calculation to isolate the contribution from the MA^+ cation (Figures 2H, S6C, S6G, S6K, and S7), and C, N, and D to zero to isolate contributions from the inorganic octahedra (Figures 2G, S6B, S6F, S6J, and S7). Diffuse scattering from the inorganic framework manifests as extended diffuse rods along the zone edge, resembling the experimental XDS, as the X-ray atomic form factors for C, N, D are small compared with those for Pb and I and contribute little intensity. The calculated $S(\mathbf{Q})$ from $CD_3ND_3^+$ shows remarkable behavior (Figures 2H, S6, and S7), namely well-defined diffuse rods along the zone edges in addition to broad, isotropic intensity. This broad, isotropic component is a result of uncorrelated MA^+ dynamics[33,36] commonly associated with the nominally cubic phases of hybrid LHPs. The presence of additional zone-edge intensity, however, shows that previously unreported intermolecular structural correlations exist in the MA^+ sublattice. These local correlations are not purely 2D, as the intensity varies along individual diffuse rods in the MA^+ $S(\mathbf{Q})$ (Figures S6 and S7). Layers of PbX_6 octahedra are sandwiched between layers of MA^+ cations; therefore, we expect the out-of-plane MA^+ structural correlations to extend at least two unit cells. Finally, the MA^+ and PbX_6 correlations are connected, as evidenced by a nonzero interference term, shown in Figure S8, which results in the alternating diffuse intensity profile observed in NDS.

The lateral size of the 2D pancakes, given by the correlation length, ξ, is obtained from the Q-linewidth of the XDS and NDS diffuse rods. We fit the intensity of one-dimensional cuts in Å^{-1} across various diffuse rods to a Lorentzian lineshape in accordance with Ornstein-Zernike theory for exponentially decaying spatial correlations:

$$S(\mathbf{q}) \propto \frac{\Gamma}{\Gamma^2 + (q - q_0)^2} \qquad \text{(Equation 1)}$$

where $\Gamma = 1/\xi$ is the half-width at half-maximum (HWHM) of the fitted Lorentzian and ξ is the correlation length.[10,37] Correlation lengths of 4–6 unit cells (~3 nm) in diameter are obtained for $MAPbBr_3$ and $MAPbI_3$, as reported in Table S1. Similar ξ are obtained from NDS and XDS, indicating that the in-plane ξ of the *MA^+ sublattice* is nearly equivalent to the 2D PbX_6 correlations. We also calculate ξ directly from the MD simulations (see Figures S9–S12 and related discussion) and find values consistent with the experiment.

MD simulations show that the 2D structural correlations are transient and diffusive, and the dynamics of the octahedral correlations are tracked in Figure 3 and Videos S1 and S2. We investigate the dynamics of the PbI_6 and MA^+ correlations by evaluating the energy dependence obtained from the dynamical structure factor $S(\mathbf{Q}, E = \hbar\omega)$, measured with neutron inelastic spectroscopy (NIS) on $MAPbI_3$ at 340 K. The $S(\mathbf{Q}, E)$ in the L = 0.5 plane, integrated from $-1 \leq E \leq 1$ meV, is shown in the right-hand panel of Figure 4A and matches that observed with NDS (Figure 2B) and that calculated from MD (left-hand panel, Figure 4B). A slice of $S(\mathbf{Q}, E)$ along the diffuse rod presented in Figure 4B shows that the intensity is centered at E = 0 meV, with no inelastic component visible. Incoherent-background-subtracted energy scans (integrated along the length of the diffuse rod) show a finite, quasielastic component, as exemplified in Figure 4D. Quasielastic scattering is a result of diffusive or relaxational motions involving small energy transfers, manifesting as a peak centered at E = 0 meV with a nonzero linewidth. The scattering is fit to a relaxational (Lorentzian) model, broadened by the resolution function, as shown in Figure 4D.

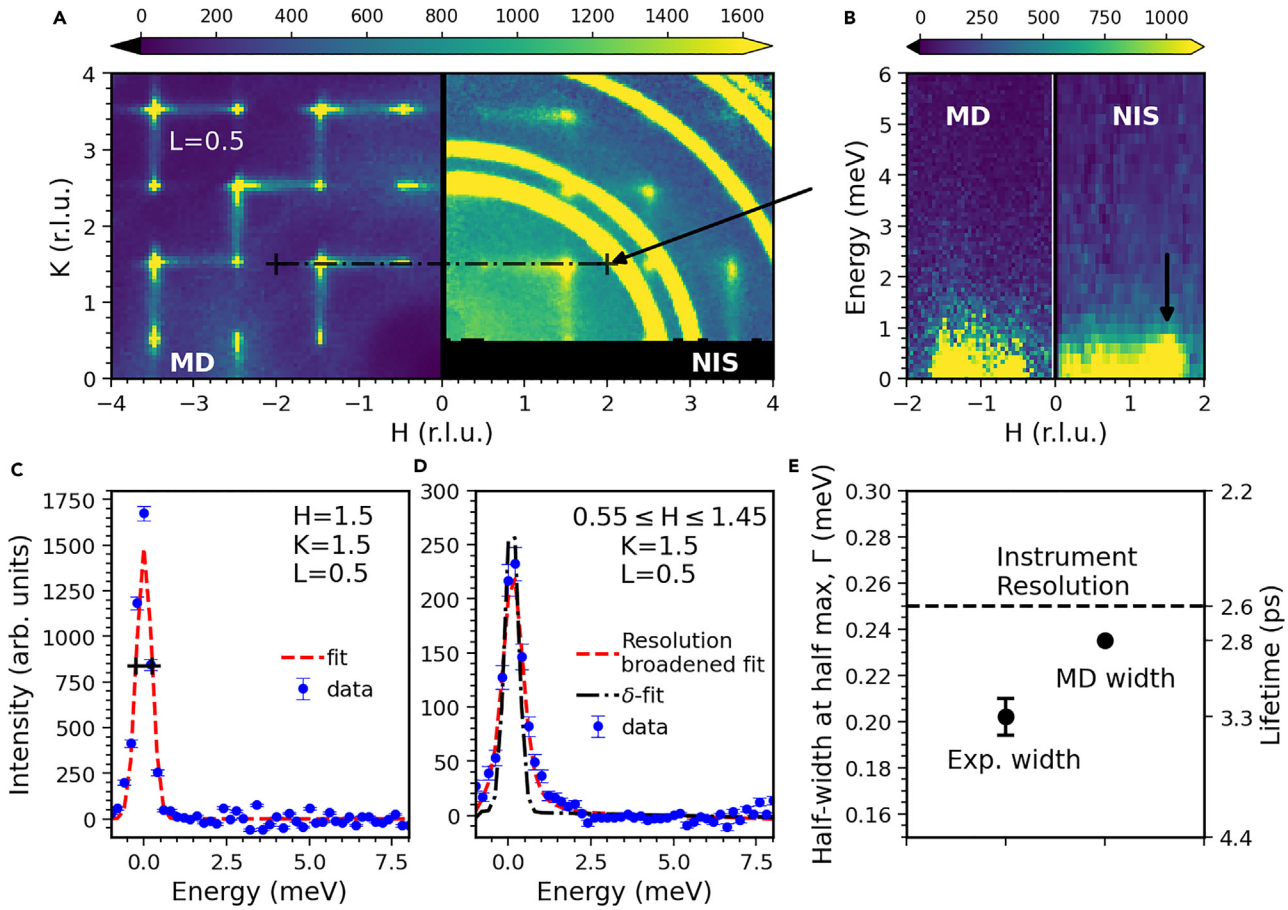

Figure 4. Energy dependence of the diffuse scattering in $MAPbI_3$

(A–D) Neutron inelastic scattering data were measured at 340 K. In the left panel of (A), the $S(\mathbf{Q})$ from MD and the experiment is integrated from $-1 \leq E \leq 1$ meV. MD $S(\mathbf{Q}, E)$ is plotted in the left panel of (B). Powder rings from the aluminum sample holder are visible in (A). Constant-$\mathbf{Q}$ scans at the R-point (C), integrated along 1.45:H:1.55, 1.45:K:1.55, 0.45:L:0.55, and along the diffuse rod (D), integrated along 0.55:H:1.45, 1.45:K:1.55, 0.45:L:0.55), are fit to Gaussian and resolution-broadened Lorentzian lineshapes with resolution linewidth of 0.5 meV FWHM, respectively (red dashed lines). The black line in (C) indicates the 0.5 meV resolution FWHM. In (D), we include the resolution lineshape (black dash-dot line), demonstrating a finite width beyond the resolution. Data in (C) and (D) follow Poisson statistics, where intensity is plotted as counts $n \pm \sqrt{n}$.

(E) The average HWHM (and corresponding lifetime) obtained from Lorentzian fits to constant-$\mathbf{Q}$ scans is plotted for experiments and MD. The dashed line represents the energy resolution of the MERLIN spectrometer. The experimental HWHM is the average ± standard deviation of fits for four separate diffuse rods.

The average energy HWHM, plotted in Figure 4E, is 0.20 ± 0.01 meV, with a corresponding lifetime $\tau = \hbar/\text{HWHM}$ of 3.25 ± 0.13 ps. Lifetimes are obtained in the same manner from the calculated $S(\mathbf{Q}, E)$, as shown in Figure S13, and the average lifetime of 2.8 ps is reported in Figure 4E. We note that these lifetimes are consistent with the mean residence time for rotations of the C–N bond in cubic $MAPbI_3$, suggesting that MA^+ reorientations are in part driven by the PbX_6 correlations.[33] Overall, the structural correlations are dynamic with finite lifetime of several picoseconds.

R-point scattering ($\mathbf{Q} = [1.5, 1.5, 0.5]$, Figure 4C) noted above has been investigated previously and is attributed to static droplets of the intermediate-temperature tetragonal phase embedded within the high-temperature cubic phase, possibly nucleating about defects.[27] We observe no inelastic scattering at the R points in both the NIS or MD $S(\mathbf{Q} = (H, 1.5, 0.5), E)$ in Figure 4B. Incoherent-background-subtracted energy scans at a constant $\mathbf{Q}$ corresponding to R points are best fit by a

Please cite this article in press as: Weadock et al., The nature of dynamic local order in $CH_3NH_3PbI_3$ and $CH_3NH_3PbBr_3$, Joule (2023), https://doi.org/10.1016/j.joule.2023.03.017

Gaussian lineshape with resolution-limited linewidth (Figure 4C), hence this scattering is static with ξ = 2 nm (Table S1), consistent with previous reports.[27] These droplets are distinct from the 2D pancakes, but we are not able to resolve the spatial distribution of these two components. We expect that both structures influence MA^+ orientation.

The appearance of small regions of a lower-temperature phase above the phase transition temperature is often a hallmark of critical scattering. For phase transitions with critical fluctuations, there is a marked jump in the scattering intensity associated with the low-temperature phase as the system is cooled through the transition.[38] We investigate the temperature dependence of the diffuse scattering in Figures S13 and S14 through the cubic-tetragonal transition temperatures for $MAPbI_3$ and $MAPbBr_3$. The intensity of the diffuse rods increases continuously on cooling through the transition; however, no significant and abrupt jump in intensity is observed. Furthermore, the 2D nature of the dynamic structural correlations is not typical of critical behavior at phase transitions. For the R-point scattering, however, there is a large jump in intensity, as the cubic R-point transforms to the Γ-point of the tetragonal phase, producing Bragg scattering. The critical nature of the R-point scattering has been addressed previously.[25,27]

We contrast our results to the 2D correlations in $CsPbBr_3$.[6] These correlations, reportedly driven by soft, overdamped, anharmonic phonons at the BZ edge, occur within the high-temperature cubic phase at 433 K. Anharmonic lattice dynamics are well documented in LHPs[34,35,39,40]; therefore, we expect that the correlations we observe in the hybrid LHPs $MAPbI_3$ and $MAPbBr_3$ arise from overdamped phonons as well. These phonons generate the non-dispersive, quasielastic intensity along the M-R BZ edge in Figure 4B. Given the existence of 2D $PbBr_6$ correlations in $CsPbBr_3$, we propose that MA^+ orientation is driven by PbX_6 tilts; the MA^+ molecules orient to favor the lowest energy configuration defined by the distorted cuboctahedral geometry of the tilted regions and electrostatic interactions between lead-halide octahedra and polar MA^+ molecules.[40,41] The dynamic intermolecular correlations, forced by octahedral correlations, have been previously unreported and likely contribute to the excellent optoelectronic properties of hybrid LHPs. Furthermore, the correlations we observe in hybrid LHPs occur at temperatures relevant to device operation and have a longer lifetime than those in $CsPbBr_3$. Therefore, we expect that this dynamic structure has a direct impact on device performance by influencing halide migration and charge carrier dynamics.

Our results show that the simple cubic phase of $MAPbI_3$ and $MAPbBr_3$ is in fact a composite structure containing dynamic 2D structural correlations and static tetragonal droplets with ξ of a few nanometers. MA^+ correlations, induced by octahedral tilts, extend 2–3 unit cells in the normal direction. The simple cubic phase is only recovered when this composite is averaged over space and time (Figures 1A–1D). It is now critical to connect the structure observed here with the remarkable properties of hybrid LHP devices. The MD potential used here has predicted optoelectronic properties and ionic conductivities that match well with experimental data,[20,42] Mayers et al. conclude that the large-amplitude, dynamic iodide displacements are the main driver of the long charge carrier lifetime. In Figure S18, we show that the $S(\mathbf{Q})$ calculated from the simulation of Mayers et al. is in excellent agreement with our calculations and experimental data, demonstrating that the same structure is present in their simulations. The large-amplitude iodide displacements likely arise from the correlations we observe. Thus, the 2D dynamic correlations are responsible

for the unique charge carrier dynamics in hybrid LHPs. Based on the above assessment, we conclude that the ionic mobility reported in Barboni and De Souza[42] is similarly impacted by the observed dynamic correlations.

Finally, we hypothesize how the dynamic correlations and static droplets contribute to the optoelectronic properties and halide migration. We expect the structure introduces spatial anisotropy into the electronic potential landscape, with a longer lifetime than variations resulting from uncorrelated dynamic disorder. MA^+ has a large electric dipole moment of 2.3 Debye along the C-N axis.[32] Uncorrelated dynamic disorder of the MA^+ sublattice, as previously reported, would generate a zero or negligible dipole moment. The MA^+ correlations observed here, however, may generate a net dipole moment, and this could lead to transient, local ferroelectric or antiferroelectric domains with lifetimes in the order of 3–6 ps. These domains influence electron-hole recombination and shift band alignment.[43,44] The dynamic structural correlations also affect ion migration. Because the lifetime of the dynamic structural correlations (3–6 ps) exceeds the calculated time between attempted halide jumps (1 ps),[45] a prefactor in calculating diffusivity, the correlations appear static and must be considered in future calculations. These correlations may impose a barrier to halide migration and reduce diffusivity.[31] The origin of the remarkable optoelectronic properties of LHPs continues to elude researchers; the local structure solved here is an important step in a complete understanding of these materials.

EXPERIMENTAL PROCEDURES

Resource availability

Lead contact

Nicholas J. Weadock.

Materials availability

This study did not generate new unique materials.

Data and code availability

The code used to calculate $S(Q, E)$ from MD datasets is available at Zenodo: https://doi.org/10.5281/zenodo.7662344. The symmetrized XDS datasets used in our analysis are available at Zenodo: https://doi.org/10.5281/zenodo.7668462, and the background subtracted NDS datasets are available at Zenodo: https://doi.org/10.5281/zenodo.7675312. Neutron inelastic scattering datasets and experimental information are available at the ISIS Neutron and Muon Source Data Journal: https://doi.org/10.5286/ISIS.E.RB2010431-1.

Single crystal growth

Materials

Methyl-d_3-amine (CD_3NH_2, 99 at. % D) was purchased from Sigma-Aldrich. Hydrobromic acid (concentrated HBr solution, 48% in water) was purchased from Acros Organics. Hydroiodic acid (concentrated HI solution, $\geq$47 % in water with $\leq$ 1.5% hypophosphorous acid) was purchased from Sigma-Aldrich. Methanol-d_4 and ethanol-d_6 were purchased from Acros Organics and Cambridge Isotope Laboratories, respectively, with Arnold et al. $\geq$99 at. % D purity. PbI_2 (99.999+%-Pb) and $PbBr_2$ (98+%, extra pure) were purchased from Strem Chemicals and Acros Organics, respectively. CH_3NH_3I and CH_3NH_3Br were purchased from Greatcell Solar Materials. All solvents were of reagent grade or higher purity and anhydrous solvents were stored over molecular sieves or used directly from a JC Meyer solvent purification system.

Please cite this article in press as: Weadock et al., The nature of dynamic local order in $CH_3NH_3PbI_3$ and $CH_3NH_3PbBr_3$, Joule (2023), https://doi.org/10.1016/j.joule.2023.03.017

Synthesis of $CD_3ND_3X_3$ (X = Br, I)

Methyl-d_3-amine was bubbled through ethanol (in a round bottom flask with flowing N_2 in the headspace) in an ice water bath under vigorous stirring for approximately 2 min. Excess concentrated HBr was subsequently added dropwise with stirring. After the solution warmed naturally to room temperature (RT), the solvent was removed under reduced pressure at 60°C. The resulting oil was re-dissolved in anhydrous ethanol and the product, CD_3NH_3Br, was precipitated as a colorless solid upon addition of the solution to cold diethyl ether. The solid was isolated by vacuum filtration and subsequently re-dispersed, sonicated, and isolated from diethyl ether three times before drying the product overnight under reduced pressure.

Solid CD_3NH_3Br was dissolved in ethanol-d_6 and stirred for 3 h at 60°C before precipitating the product in anhydrous diethyl ether and removing excess solvent under reduced pressure. This hydrogen-deuterium exchange was repeated twice more before finally isolating and drying the product, CD_3ND_3Br, at 65°C overnight.

The synthesis of CD_3ND_3I followed an analogous procedure as for CD_3ND_3Br, except for the substitutions of: ethanol (or ethanol-d_6 during the exchange) for methanol (or methanol-d_4), and concentrated HBr for concentrated HI.

Crystallization of $CD_3ND_3PbBr_3$

Solid CD_3ND_3Br (0.235 g, 2 mmol) and $PbBr_2$ (0.731 g, 2 mmol) were combined in 2 mL of anhydrous dimethylformamide and the mixture was sonicated for 20 min. Once dissolved, the solution was passed through a 0.22-μm hydrophilic PTFE filter and transferred to an oil bath at 78°C. Crystals of $CD_3ND_3PbBr_3$ slowly nucleated at the interface between the solution and the surface of the vial as the temperature increased slowly (1°C–3°C h^{-1}) from 78°C (up to 85°C–100°C). Crystals were isolated from the hot solution and the residual precursor solution was quickly removed from the surface of the crystal. Large crystals ($\geq$200 mg) were obtained by isolating small crystals (25–50 mg) as seeds and re-filtering the precursor solution into a fresh vial with one seed crystal and quickly transferring back to the oil bath at 78°C. Repeating the temperature ramp described above resulted in large crystal growth after a period of minor re-dissolution from the seed.

Crystallization of $CH_3NH_3PbBr_3$

A 1 M solution of CH_3NH_3Br and $PbBr_2$ in anhydrous dimethylformamide was prepared and sonicated for 1 h. Then 1 mL of the precursor solution was passed through a glass microfiber filter and transferred to a shell vial. The shell vial was placed inside a larger vial containing 4 mL of dichloromethane, the anti-solvent for the vapor diffusion crystallization, and sealed. Millimeter-scale $CH_3NH_3PbBr_3$ crystals formed over the course of hours to days at RT.

Crystallization of $CD_3ND_3PbI_3$ and $CH_3NH_3PbI_3$

Solid CD_3ND_3I (0.594 g, 3.6 mmol) and PbI_2 (1.66 g, 3.6 mmol) were combined in 3 mL of anhydrous γ-butyrolactone and dissolved at 70°C with stirring. The solution was hot-filtered through a through a 0.22 μm PTFE filter and immediately transferred to an oil bath at 70°C. The temperature was increased to 110°C over the course of approximately 2 h, followed by a slow ramp (1°C–3°C h^{-1}) up to 120°C–130°C. Crystals were isolated and re-seeded as described for $CD_3ND_3PbBr_3$ to reach the desired size.

The crystallization of $CH_3NH_3PbI_3$ followed an analogous procedure as for $CD_3ND_3PbI_3$, except for the substitution of CD_3ND_3I for CH_3NH_3I.

Please cite this article in press as: Weadock et al., The nature of dynamic local order in $CH_3NH_3PbI_3$ and $CH_3NH_3PbBr_3$, Joule (2023), https://doi.org/10.1016/j.joule.2023.03.017

Diffuse X-ray scattering

Reciprocal space maps, including Bragg and diffuse scattering contributions, were collected in transmission geometry at the Advanced Photon Source Sector 6-ID-D using monochromatic 86.9 keV X rays. This X-ray scattering is inherently energy integrated, incorporating contributions from both static and thermal diffuse disorder. Single crystal samples of $CD_3ND_3PbI_3$, $CH_3NH_3PbI_3$, and $CH_3NH_3PbBr_3$, $\sim 500\ \mu m$ in size, were mounted on the tip of Kapton capillaries. At each temperature, the sample was rotated 365° at $1°s^{-1}$ with images collected every 0.1 s on a Pilatus 2M CdTe area detector. Sample temperatures were varied between 150 and 300 K with an Oxford N-HeliX Cryostream and 300–360 K with a hot nitrogen blower. The raw images are first processed with a peak finding algorithm to determine and refine an orientation matrix, and then rebinned into a reciprocal space volume $\pm$ 10 reciprocal lattice units (r.l.u.) along each reciprocal lattice vector using the CCTW reduction workflow.[5,46] The dataset is symmetrized using cubic point group operations to remove missing data resulting from gaps between detector pixel banks.

Sample damage is evident from changes in the scattering intensity with prolonged exposure. The damage thresholds were determined by identifying the onset of additional scattering intensity in subsequent measurements of the same sample at constant temperature. In $MAPbI_3$, damage is apparent after 90 min of measurement time, including time when the shutter is off in between each rotation for data collection. Therefore, all diffuse scattering analyzed here were collected on a fresh sample within 90 min.

Diffuse neutron scattering

NDS measurements were performed on the CORELLI spectrometer at the Spallation Neutron Source at Oak Ridge National Lab in Oak Ridge, Tennessee, USA.[15,17] Deuterated $MAPbBr_3$ (300, 350 mg, rectangular prism) and $MAPbI_3$ (220 mg, rhombic dodecahedron) crystals were used to reduce incoherent background contributions from hydrogen. The crystals were mounted in a closed-cycle refrigerator (CCR) cryostat and oriented in the (HK0) scattering plane. The incident neutron energies range from 10 to 200 meV, and the 2θ coverage spans $-30°$ to 145°. $MAPbBr_3$ scattering data were collected from 150–300 K for 4–6 h per temperature, and $MAPbI_3$ scattering data were collected from 300 to 400 K at 12 h per temperature to account for smaller sample size and increased background from the thermal shielding. Diffuse scattering volumes $\pm$6 r.l.u. along each reciprocal lattice vector were obtained by reducing the raw data using defined workflows implemented in MANTID.[47] The contributions from inelastic scattering are removed by implementing the cross-correlation technique in the MANTID reduction workflow. The cross-correlation chopper selects elastically scattered neutrons within a resolution bandwidth of 0.9 meV full width at half-maximum (FWHM).[17] Background artefacts including the aluminum sample enclosure are removed by subtracting the highest temperature datasets (300 K for $MAPbBr_3$, 400 K for $MAPbI_3$), normalized by the Bragg peaks, where little to no diffuse scattering is detected.

Neutron inelastic scattering

Neutron inelastic scattering measurements were performed on the Merlin direct geometry chopper spectrometer at the ISIS Neutron and Muon source at the Rutherford Appleton Laboratory in Didcot, UK.[48] A deuterated single crystal of $MAPbI_3$ weighing 698 mg was oriented in the (HKK) scattering plane and mounted in a Brookhaven-style aluminum sample can. Temperature control was performed using a CCR with heaters attached directly to the sample can. Three incident energies of 11, 22, and 65 meV were selected by utilizing the repetition rate multiplication mode with the

Please cite this article in press as: Weadock et al., The nature of dynamic local order in $CH_3NH_3PbI_3$ and $CH_3NH_3PbBr_3$, Joule (2023), https://doi.org/10.1016/j.joule.2023.03.017

Fermi chopper set to 250 Hz. The $S(\mathbf{Q}, E)$ was collected at 340 K by rotating the sample 120° in 0.5° steps, and a radial collimator was used to reduce scattering from the aluminum sample can. Data reduction was performed using the HORACE data reduction suite and analyzed with Phonon Explorer and the National Institute of Standards and Technology (NIST) Center for Neutron Research (NCNR) Data Analysis and Visualization Environment (DAVE) software packages.[49–51]

Energy scans for linewidth analysis were sliced from the 11 meV incident energy $S(\mathbf{Q}, E)$ dataset. The resolution linewidth of this dataset was determined from constant-$\mathbf{Q}$ scans at $\mathbf{Q}$ values unique to the aluminum Debye-Scherrer rings. Several constant-$\mathbf{Q}$ scans obtained in this manner were fit to a Gaussian lineshape with constant background to obtain an average resolution linewidth of 0.5 meV FWHM. A representative constant-$\mathbf{Q}$ scan was used as the resolution function in subsequent analyses. The incoherent background was determined from constant-$\mathbf{Q}$ scans at $\mathbf{Q}$ values which contain only incoherent scattering with no contributions from diffuse rods, Bragg peaks, or aluminum Debye-Scherrer rings. Several background scans were averaged, then subtracted from the constant-$\mathbf{Q}$ scans along the diffuse rods and at the R-point to remove the incoherent background contribution and isolate the dynamics associated with these features.

Additional high-resolution neutron spectroscopy was performed on the cold neutron triple-axis spectrometer (SPINS) at the NCNR in Gaithersburg, MD, USA. The same deuterated single crystal of $MAPbI_3$ weighing 698 mg was oriented in the (HKK) scattering plane and mounted in a Brookhaven-style aluminum sample can. Constant-$\mathbf{Q}$ scans, in which we vary the energy transfer while maintaining constant momentum transfer $\mathbf{Q}$, were performed with a fixed final energy $E_F = 5$ meV. We compare constant-$\mathbf{Q}$ scans taken along $\mathbf{Q} = (2, k, 0)$ and at $\mathbf{Q} = (1.5, 0, 0)$ at 300 and 140 K, to constant-$\mathbf{Q}$ cuts calculated from the MD $S(\mathbf{Q}, E)$ as a way to validate the calculations.

Molecular dynamics simulations

MD trajectories for $MAPbI_3$ are generated using identical simulations to those in Zhu and Ertekin.[40] We checked our calculations using both the mass of hydrogen and the mass of deuterium in the simulation and found no noticeable difference. We used a 20×20×20 super-cell that is based on the 12-atom pseudocubic unit cell with cell length $a \approx 6.3$ Å. The simulations were done in the Large-scale Atomic/Molecular Massively Parallel Simulator (LAMMPS) package.[52] The inter-atomic potential is from Mattoni et al.[53] Trajectories were integrated using a 0.25 fs time step throughout. For the first 20 ps, the system was thermalized in the NPT ensemble at 345 K and 0 Pa, then it was equilibrated for another 20 ps in the NVE ensemble. After equilibration, the equations of motion were integrated for 20 ns and trajectories were written to a file every 25 fs.

S(Q,E) calculations

The dynamical structure factor, $S(\mathbf{Q}, E)$, can be calculated from MD. Given a set of suitably accurate trajectories, $\mathbf{r}_i(t)$, $S(\mathbf{Q}, E)$ can be evaluated directly as

$$S(\mathbf{Q}, E) = \left| \sum_i^N f_i(Q) \int \exp\left(i\left(\mathbf{Q}\cdot\mathbf{r}_i(t) - \frac{E}{\hbar} t \right) \right) dt \right|^2 \qquad \text{(Equation 2)}$$

See the supplemental information and references therein[54–61] for a derivation of Equation 2. The theoretical $S(\mathbf{Q}, E)$ calculations were done with a Python code developed by us.[62] The calculated $S(\mathbf{Q}, E)$ is weighted by X-ray atomic form factors

or thermal neutron scattering lengths for direct comparison to experimental data.[54,57] If the experiment uses neutrons, $f_i(Q) \equiv b_i$ is the Q-independent scattering length; if the experiment uses X rays, $f_i(Q)$ is the Q-dependent atomic form factor where Q is the magnitude of momentum transferred, $\mathbf{Q}$, from the incident beam of particles into the material. E is the energy transferred into the material and the sum runs over all N atoms.

The reciprocal space resolution from MD is $\Delta Q \approx 0.05 \text{Å}^{-1}$. We do not integrate the calculation over reciprocal space unless otherwise specified, so the pixels in theoretical $S(\mathbf{Q}, E)$ plots have this spacing. In order to ensure we are far from the transient thermalization regime in MD, we only sample the end of the simulation. We split the last 0.25 ns of the simulation into 15 blocks that are $\approx$17 ps long; $S(\mathbf{Q}, E)$ is then calculated from 8 non-consecutive blocks and averaged over them. For 17 ps blocks with a 50 fs sampling interval, the energy resolution is about 0.24 meV and the maximum resolvable energy is 41.4 meV.

To compare to the experimental NDS data in Figure 2, theoretical $S(\mathbf{Q}, E)$ is integrated between $\pm$1 meV, which is comparable to the resolution in the experiment. To compare to the experimental XDS data in Figure 2, theoretical $S(\mathbf{Q}, E)$ is integrated between $\pm$2 meV. To compare with NIS data in Figure 3, both the experimental and theoretical $S(\mathbf{Q}, E)$ are integrated $\pm$1 meV. Anywhere that purely theoretical data are compared, the integration is $\pm$1 meV. For excitations (e.g., Figure 4B), the theoretical $S(\mathbf{Q}, E)$ is not integrated over energy; the MD energy resolution is set by the length of the trajectory sampled in the calculation.

The workflow and analysis outlined above was performed on MD simulations of deuterated $MAPbI_3$ and no significant differences were observed. The protonated results are used in the main text for direct comparison to the experimental measurements.

Plotting

The unit cells in Figures 1A and 1B were plotted in VESTA.[63] The volumetric plot in Figure 1E was made in MAYAVI.[64] Most other plots were made using the matplotlib package for Python.[65]

SUPPLEMENTAL INFORMATION

Supplemental information can be found online at https://doi.org/10.1016/j.joule.2023.03.017.

ACKNOWLEDGMENTS

The authors acknowledge helpful discussions with Xixi Qin, Volker Blum, and Alex Zunger. We thank Maximilian Schilcher and David Egger (both TU Munich) for providing their MD simulations for comparison. This work (X-ray and neutron scattering, interpretation) was supported by the Center for Hybrid Organic Inorganic Semiconductors for Energy and Energy Frontier Research Center funded by the Office of Basic Energy Sciences, an office of science within the US Department of Energy (DOE). J.A.V. acknowledges fellowship support from the Stanford University Office of the Vice Provost of Graduate Education and the National Science Foundation Graduate Research Fellowship Program under grant no. DGE – 1656518 (sample preparation, NDS and XDS data collection). H.I.K. acknowledges funding through the DOE Office of Basic Energy Sciences, Division of Materials Science and Engineering under contract no. DE-AC02-76SF0051 (sample preparation).

B.A. and E.E. acknowledge funding from the National Science Foundation award OAC 2118201 (MD simulations). T.C.S. and D.R. acknowledge funding by the DOE Office of Basic Energy Sciences, Office of Science under contract no. DE-SC0006939 (NIS data collection, S(Q,E) calculations, interpretation). A.M.R. acknowledges support from the National Science Foundation, Science and Technology Centers Program under grant number DMR-2019444 (supplemental MD simulations). A portion of this work (S(Q) calculations) used the Summit supercomputer, which is supported by the National Science Foundation (awards ACI-1532235 and ACI-1532236), the University of Colorado Boulder, and Colorado State University. The Summit supercomputer is a joint effort of the University of Colorado Boulder and Colorado State University. A portion of this research used resources at the Spallation Neutron Source, a DOE Office of Science User Facility operated by the Oak Ridge National Laboratory. Use of the Advanced Photon Source at Argonne National Laboratory was supported by the US Department of Energy, Office of Science, Office of Basic Energy Sciences under contract no. DE-AC02-06CH11357. Experiments at the ISIS Pulsed Neutron and Muon Source were supported by a beamtime allocation from the Science and Technology Facilities Council. Any mention of commercial products here is for information only; it does not imply recommendation or endorsement by the National Institute of Standards and Technology.

AUTHOR CONTRIBUTIONS

Conceptualization, N.J.W., H.-G.S., and M.F.T.; methodology, N.J.W., T.C.S., B.A., and E.E.; investigation, N.J.W., T.C.S., J.A.V., H.-G.S., P.M.G., F.Y., M.J.K., D.V., and D.R.; resources, J.A.V., A.G.-P., I.C.S., B.A., A.M.R., H.I.K., E.E., F.Y., M.J.K., and D.V.; data curation, B.A., A.M.R., E.E., F.Y., M.J.K., and D.V.; visualization, N.J.W. and T.C.S.; writing – original draft, N.J.W., T.C.S., and J.A.V.; writing – review & editing, all authors; supervision, D.R. and M.F.T.; funding acquisition, M.F.T., D.R., E.E., H.I.K., and A.M.R.

DECLARATION OF INTERESTS

The authors declare no competing interests.

INCLUSION AND DIVERSITY

We support inclusive, diverse, and equitable conduct of research. One or more of the authors of this paper self-identifies as an underrepresented ethnic minority in their field of research or within their geographical location. One or more of the authors of this paper self-identifies as a gender minority in their field of research. One or more of the authors of this paper received support from a program designed to increase minority representation in their field of research.

Received: August 15, 2022
Revised: January 9, 2023
Accepted: March 22, 2023
Published: April 17, 2023

REFERENCES

1. Ashcroft, N.W., and Mermin, N.D. (2000). Solid State Physics (Harcourt Publishers).

2. Kittel, C. (2019). Introduction to Solid State Physics (John Wiley & Sons).

3. Clément, R.J., Lun, Z., and Ceder, G. (2020). Cation-disordered rocksalt transition metal oxides and oxyfluorides for high energy lithium-ion cathodes. Energy Environ. Sci. *13*, 345–373. https://doi.org/10.1039/C9EE02803J.

4. Krogstad, M.J., Gehring, P.M., Rosenkranz, S., Osborn, R., Ye, F., Liu, Y., Ruff, J.P.C., Chen, W., Wozniak, J.M., Luo, H., et al. (2018). The relation of local order to material properties in relaxor ferroelectrics. Nat. Mater. *17*, 718–724. https://doi.org/10.1038/s41563-018-0112-7.

5. Krogstad, M.J., Rosenkranz, S., Wozniak, J.M., Jennings, G., Ruff, J.P.C., Vaughey, J.T., and Osborn, R. (2020). Reciprocal space imaging of ionic correlations in intercalation compounds.

Nat. Mater. *19*, 63–68. https://doi.org/10.1038/s41563-019-0500-7.

6. Lanigan-Atkins, T., He, X., Krogstad, M.J., Pajerowski, D.M., Abernathy, D.L., Xu, G.N.M.N., Xu, Z., Chung, D.Y., Kanatzidis, M.G., Rosenkranz, S., et al. (2021). Two-dimensional overdamped fluctuations of the soft perovskite lattice in CsPbBr3. Nat. Mater. *20*, 977–983. https://doi.org/10.1038/s41563-021-00947-y.

7. Roth, N., and Iversen, B.B. (2019). Solving the disordered structure of β-Cu2-xSe using the three-dimensional difference pair distribution function. Acta Crystallogr. A Found. Adv. *75*, 465–473. https://doi.org/10.1107/S2053273319004820.

8. Roth, N., Zhu, T., and Iversen, B.B. (2020). A simple model for vacancy order and disorder in defective half-Heusler systems. IUCrJ *7*, 673–680. https://doi.org/10.1107/S2052252520005977.

9. Simonov, A., De Baerdemaeker, T., Boström, H.L.B., Ríos Gómez, M.L., Gray, H.J., Chernyshov, D., Bosak, A., Bürgi, H.B., and Goodwin, A.L. (2020). Hidden diversity of vacancy networks in Prussian Blue analogues. Nature *578*, 256–260. https://doi.org/10.1038/s41586-020-1980-y.

10. Xu, G., Zhong, Z., Hiraka, H., and Shirane, G. (2004). Three-dimensional mapping of diffuse scattering in Pb $(Zn_{1/3}\,Nb_{2/3})\,O_3 - xPbTiO_3$. Phys. Rev. B *70*, 174109. https://doi.org/10.1103/PhysRevB.70.174109.

11. Welberry, T.R., and Weber, T. (2016). One hundred years of diffuse scattering. Crystallogr. Rev. *22*, 2–78. https://doi.org/10.1080/0889311X.2015.1046853.

12. Roth, N., May, A.F., Ye, F., Chakoumakos, B.C., and Iversen, B.B. (2018). Model-free reconstruction of magnetic correlations in frustrated magnets. IUCrJ *5*, 410–416. https://doi.org/10.1107/S2052252518006590.

13. Morgan, Z.J., Zhou, H.D., Chakoumakos, B.C., and Ye, F. (2021). Rmc-discord: reverse Monte Carlo refinement of diffuse scattering and correlated disorder from single crystals. J. Appl. Crystallogr. *54*, 1867–1885. https://doi.org/10.1107/S1600576721010141.

14. Proffen, T., and Kim, H. (2009). Advances in total scattering analysis. J. Mater. Chem. *19*. 5078-88. https://doi.org/10.1039/B821178G.

15. Rosenkranz, S., and Osborn, R. (2008). Corelli: efficient single crystal diffraction with elastic discrimination. Pramana *71*, 705–711. https://doi.org/10.1007/s12043-008-0259-x.

16. Simonov, A., Weber, T., and Steurer, W. (2014). Yell: A computer program for diffuse scattering analysis via three-dimensional delta pair distribution function refinement. J. Appl. Crystallogr. *47*, 1146–1152. https://doi.org/10.1107/S1600576714008668.

17. Ye, F., Liu, Y., Whitfield, R., Osborn, R., and Rosenkranz, S. (2018). Implementation of cross correlation for energy discrimination on the time-of-flight spectrometer CORELLI. J. Appl. Crystallogr. *51*, 315–322. https://doi.org/10.1107/S160057671800403X.

18. Støckler, K.A.H., Roth, N., Grønbech, T.B.E., and Iversen, B.B. (2022). Epitaxial intergrowths and local oxide relaxations in natural bixbyite Fe2-xMnxO3. IUCrJ *9*, 523–532. https://doi.org/10.1107/S2052252522006315.

19. Egger, D.A., Bera, A., Cahen, D., Hodes, G., Kirchartz, T., Kronik, L., Lovrincic, R., Rappe, A.M., Reichman, D.R., and Yaffe, O. (2018). What remains unexplained about the properties of halide perovskites? Adv. Mater. *30*, e1800691. https://doi.org/10.1002/adma.201800691.

20. Mayers, M.Z., Tan, L.Z., Egger, D.A., Rappe, A.M., and Reichman, D.R. (2018). How lattice and charge fluctuations control carrier dynamics in halide perovskites. Nano Lett. *18*, 8041–8046. https://doi.org/10.1021/acs.nanolett.8b04276.

21. Swainson, I.P., Hammond, R.P., Soullière, C., Knop, O., and Massa, W. (2003). Phase transitions in the perovskite methylammonium lead bromide, CH3ND3PbBr3. J. Solid State Chem. *176*, 97–104. https://doi.org/10.1016/S0022-4596(03)00352-9.

22. Weller, M.T., Weber, O.J., Henry, P.F., Di Pumpo, A.M.D., and Hansen, T.C. (2015). Complete structure and cation orientation in the perovskite photovoltaic methylammonium lead iodide between 100 and 352 K. Chem. Commun. (Camb) *51*, 4180–4183. https://doi.org/10.1039/C4CC09944C.

23. Whitfield, P.S., Herron, N., Guise, W.E., Page, K., Cheng, Y.Q., Milas, I., and Crawford, M.K. (2016). Structures, phase transitions and tricritical behavior of the hybrid perovskite methyl ammonium lead iodide. Sci. Rep. *6*, 35685. https://doi.org/10.1038/srep35685.

24. Beecher, A.N., Semonin, O.E., Skelton, J.M., Frost, J.M., Terban, M.W., Zhai, H., Alatas, A., Owen, J.S., Walsh, A., and Billinge, S.J.L. (2016). Direct observation of dynamic symmetry breaking above room temperature in methylammonium lead iodide perovskite. ACS Energy Lett. *1*, 880–887. https://doi.org/10.1021/acsenergylett.6b00381.

25. Comin, R., Crawford, M.K., Said, A.H., Herron, N., Guise, W.E., Wang, X., Whitfield, P.S., Jain, A., Gong, X., McGaughey, A.J.H., et al. (2016). Lattice dynamics and the nature of structural transitions in organolead halide perovskites. Phys. Rev. B *94*, 094301. https://doi.org/10.1103/PhysRevB.94.094301.

26. Laurita, G., Fabini, D.H., Stoumpos, C.C., Kanatzidis, M.G., and Seshadri, R. (2017). Chemical tuning of dynamic cation off-centering in the cubic phases of hybrid tin and lead halide perovskites. Chem. Sci. *8*, 5628–5635. https://doi.org/10.1039/C7SC01429E.

27. Weadock, N.J., Gehring, P.M., Gold-Parker, A., Smith, I.C., Karunadasa, H.I., and Toney, M.F. (2020). Test of the dynamic-domain and critical scattering hypotheses in cubic methylammonium lead triiodide. Phys. Rev. Lett. *125*, 075701. https://doi.org/10.1103/PhysRevLett.125.075701.

28. Zhao, X.-G., Dalpian, G.M., Wang, Z., and Zunger, A. (2020). Polymorphous nature of cubic halide perovskites. Phys. Rev. B *101*, 155137. https://doi.org/10.1103/PhysRevB.101.155137.

29. Guo, Y., Yaffe, O., Paley, D.W., Beecher, A.N., Hull, T.D., Szpak, G., Owen, J.S., Brus, L.E., and Pimenta, M.A. (2017). Interplay between organic cations and inorganic framework and incommensurability in hybrid lead-halide perovskite $CH_3NH_3PbBr_3$. Phys. Rev. Mater. *1*, 042401. https://doi.org/10.1103/PhysRevMaterials.1.042401.

30. Yuan, Y., and Huang, J. (2016). Ion migration in organometal trihalide perovskite and its impact on photovoltaic efficiency and stability. Acc. Chem. Res. *49*, 286–293. https://doi.org/10.1021/acs.accounts.5b00420.

31. Holekevi Chandrappa, M.L., Zhu, Z., Fenning, D.P., and Ong, S.P. (2021). Correlated octahedral rotation and organic cation reorientation assist halide ion migration in lead halide perovskites. Chem. Mater. *33*, 4672–4678. https://doi.org/10.1021/acs.chemmater.1c01175.

32. Chen, T., Chen, W.L., Foley, B.J., Lee, J., Ruff, J.P.C., Ko, J.Y.P., Brown, C.M., Harriger, L.W., Zhang, D., Park, C., et al. (2017). Origin of long lifetime of band-edge charge carriers in organic–inorganic lead iodide perovskites. Proc. Natl. Acad. Sci. USA *114*, 7519–7524. https://doi.org/10.1073/pnas.1704421114.

33. Chen, T., Foley, B.J., Ipek, B., Tyagi, M., Copley, J.R.D., Brown, C.M., Choi, J.J., and Lee, S.-H. (2015). Rotational dynamics of organic cations in the $CH_3NH_3PbI_3$ perovskite. Phys. Chem. Chem. Phys. *17*, 31278–31286. https://doi.org/10.1039/C5CP05348J.

34. Ferreira, A.C., Létoublon, A., Paofai, S., Raymond, S., Ecolivet, C., Rufflé, B., Cordier, S., Katan, C., Saidaminov, M.I., Zhumekenov, A.A., et al. (2018). Elastic softness of hybrid lead halide perovskites. Phys. Rev. Lett. *121*, 085502. https://doi.org/10.1103/PhysRevLett.121.085502.

35. Gold-Parker, A., Gehring, P.M., Skelton, J.M., Smith, I.C., Parshall, D., Frost, J.M., Karunadasa, H.I., Walsh, A., and Toney, M.F. (2018). Acoustic phonon lifetimes limit thermal transport in methylammonium lead iodide. Proc. Natl. Acad. Sci. USA *115*, 11905–11910. https://doi.org/10.1073/pnas.1812227115.

36. Leguy, A.M.A., Frost, J.M., McMahon, A.P., Sakai, V.G., Kochelmann, W., Law, C., Li, X., Foglia, F., Walsh, A., O'Regan, B.C., et al. (2015). The dynamics of methylammonium ions in hybrid organic–inorganic perovskite solar cells. Nat. Commun. *6*, 7124. https://doi.org/10.1038/ncomms8124.

37. Vale, J.G., Boseggia, S., Walker, H.C., Springell, R.S., Hunter, E.C., Perry, R.S., Collins, S.P., and McMorrow, D.F. (2019). Critical fluctuations in the spin–orbit Mott insulator $Sr_3Ir_2O_7$. J. Phys. Condens. Matter *31*, 185803. https://doi.org/10.1088/1361-648X/ab0471.

38. Stirling, W.G., and Perry, S.C. (1996). Critical scattering. In Introduction Neutron Scattering. Lecture Notes of the Introductory Course 1st European Conference on Neutron Scattering (ECNS '96) (Paul Scherrer Institut), pp. 86–102.

39. Songvilay, M., Giles-Donovan, N., Bari, M., Ye, Z.G., Minns, J.L., Green, M.A., Xu, G., Gehring, P.M., Schmalzl, K., Ratcliff, W.D., et al. (2019). Common acoustic phonon lifetimes in inorganic and hybrid lead halide perovskites. Phys. Rev. Mater. *3*, 093602. https://doi.org/10.1103/PhysRevMaterials.3.093602.

40. Zhu, T., and Ertekin, E. (2019). Mixed phononic and non-phononic transport in hybrid lead halide perovskites: glass-crystal duality, dynamical disorder, and anharmonicity. Energy Environ. Sci. *12*, 216–229. https://doi.org/10.1039/C8EE02820F.

41. Lahnsteiner, J., Kresse, G., Kumar, A., Sarma, D.D., Franchini, C., and Bokdam, M. (2016). Room-temperature dynamic correlation between methylammonium molecules in lead-iodine based perovskites: an ab initio molecular dynamics perspective. Phys. Rev. B *94*, 214114. https://doi.org/10.1103/PhysRevB.94.214114.

42. Barboni, D., and De Souza, R.A.D. (2018). The thermodynamics and kinetics of iodine vacancies in the hybrid perovskite methylammonium lead iodide. Energy Environ. Sci. *11*, 3266–3274. https://doi.org/10.1039/C8EE01697F.

43. Bi, F., Markov, S., Wang, R., Kwok, Y., Zhou, W., Liu, L., Zheng, X., Chen, G., and Yam, C. (2017). Enhanced photovoltaic properties induced by ferroelectric domain structures in organometallic halide perovskites. J. Phys. Chem. C *121*, 11151–11158. https://doi.org/10.1021/acs.jpcc.7b03091.

44. Liu, Y., Collins, L., Proksch, R., Kim, S., Watson, B.R., Doughty, B., Calhoun, T.R., Ahmadi, M., Ievlev, A.V., Jesse, S., et al. (2018). Chemical nature of ferroelastic twin domains in $CH_3NH_3PbI_3$ perovskite. Nat. Mater. *17*, 1013–1019. https://doi.org/10.1038/s41563-018-0152-z.

45. Frost, J.M., and Walsh, A. (2016). What is moving in hybrid halide perovskite solar cells? Acc. Chem. Res. *49*, 528–535. https://doi.org/10.1021/acs.accounts.5b00431.

46. Jennings, G. (2016). CCTW Crystal Coordinate Transformation Workflow. https://sourceforge.net/projects/cctw/.

47. Arnold, O., Bilheux, J.C., Borreguero, J.M., Buts, A., Campbell, S.I., Chapon, L., Doucet, M., Draper, N., Ferraz Leal, R., Gigg, M.A., et al. (2014). Mantid—data analysis and visualization package for neutron scattering and μ SR experiments. Nucl. Instrum. Methods Phys. Res. A *764*, 156–166. https://doi.org/10.1016/j.nima.2014.07.029.

48. Bewley, R.I., Eccleston, R.S., McEwen, K.A., Hayden, S.M., Dove, M.T., Bennington, S.M., Treadgold, J.R., and Coleman, R.L.S. (2006). MERLIN, a new high count rate spectrometer at ISIS. Phys. B *385*, 1029–1031. https://doi.org/10.1016/j.physb.2006.05.328.

49. Azuah, R.T., Kneller, L.R., Qiu, Y., Tregenna-Piggott, P.L., Brown, C.M., Copley, J.R.D., and Dimeo, R.M. (2009). DAVE: A comprehensive software suite for the reduction, visualization, and analysis of low energy neutron spectroscopic data. J. Res. Natl. Inst. Stand. Technol. *114*, 341–358. https://doi.org/10.6028/jres.114.025.

50. Ewings, R.A., Buts, A., Le, M.D., van Duijn, J., Bustinduy, I., and Perring, T.G. (2016). Horace: software for the analysis of data from single crystal spectroscopy experiments at time-of-flight neutron instruments. Nucl. Instrum. Methods Phys. Res. A *834*, 132–142. https://doi.org/10.1016/j.nima.2016.07.036.

51. Reznik, D., and Ahmadova, I. (2020). Automating analysis of neutron scattering time-of-flight single crystal phonon data. Quantum Beam Sci. *4*, 41. https://doi.org/10.3390/qubs4040041.

52. Plimpton, S. (1995). Fast parallel algorithms for short-range molecular dynamics. J. Comp. Phys. *117*, 1–19. https://doi.org/10.1006/jcph.1995.1039.

53. Mattoni, A., Filippetti, A., Saba, M.I., and Delugas, P. (2015). Methylammonium rotational dynamics in lead halide perovskite by classical molecular dynamics: the role of temperature. J. Phys. Chem. C *119*, 17421–17428. https://doi.org/10.1021/acs.jpcc.5b04283.

54. Brown, P.J., Fox, A.G., Maslen, E.N., O'Keefe, M.A., and Willis, B.T.M. (2006). Intensity of diffracted intensitieschapter 6.1. In International Tables for Crystallography (Wiley), pp. 554–595. https://doi.org/10.1107/97809553602060000600.

55. Dove, M.T., and Dove, M.T. (1993). Introduction to Lattice Dynamics (Cambridge University Press). https://doi.org/10.1017/CBO9780511619885.

56. Harrelson, T.F., Dettmann, M., Scherer, C., Andrienko, D., Moulé, A.J., and Faller, R. (2021). Computing inelastic neutron scattering spectra from molecular dynamics trajectories. Sci. Rep. *11*, 7938. https://doi.org/10.1038/s41598-021-86771-5.

57. Hazemann, I., Dauvergne, M.T., Blakeley, M.P., Meilleur, F., Haertlein, M., Van Dorsselaer, A., Mitschler, A., Myles, D.A., and Podjarny, A. (2005). High-resolution neutron protein crystallography with radically small crystal volumes: application of perdeuteration to human aldose reductase. Acta Crystallogr. D Biol. Crystallogr. *61*, 1413–1417. https://doi.org/10.1107/S0907444905024285.

58. Squires, G.L. (2012). Introduction to the Theory of Thermal Neutron Scattering (Cambridge University Press). https://doi.org/10.1017/CBO9781139107808.

59. Van Hove, L. (1954). Correlations in space and time and born approximation scattering in systems of interacting particles. Phys. Rev. *95*, 249–262. https://doi.org/10.1103/PhysRev.95.249.

60. Xiong, S., Selli, D., Neogi, S., and Donadio, D. (2017). Native surface oxide turns alloyed silicon membranes into nanophononic metamaterials with ultralow thermal conductivity. Phys. Rev. B *95*, 180301. https://doi.org/10.1103/PhysRevB.95.180301.

61. Zushi, T., Ohmori, K., Yamada, K., and Watanabe, T. (2015). Effect of a sio^2 layer on the thermal transport properties of <100> si nanowires: a molecular dynamics study. Phys. Rev. B *91*, 115308. https://doi.org/10.1103/PhysRevB.91.115308.

62. Sterling T.C. Pynamic structure factor. 2021; https://github.com/tyst3273/pynamic-structure-factor.

63. Momma, K., and Izumi, F. (2011). Vesta 3 for three-dimensional visualization of crystal, volumetric and morphology data. J. Appl. Crystallogr. *44*, 1272–1276. https://doi.org/10.1107/S0021889811038970.

64. Ramachandran, P., and Varoquaux, G. (2011). Mayavi: 3d visualization of scientific data. Comput. Sci. Eng. *13*, 40–51. https://doi.org/10.1109/MCSE.2011.35.

65. Hunter, J.D. (2007). Matplotlib: a 2d graphics environment. Comput. Sci. Eng. *9*, 90–95. https://doi.org/10.1109/MCSE.2007.55.